Supplementary Material: Full-field single-shot measurement of beam self-cleaning dynamics in graded-index multimode fibers

1. Calibration of the far-field for modal decomposition

To enable accurate modal decomposition of the reconstructed output fields, we calibrated the spatial frequency scale of the far-field intensity pattern using speckled beam distributions measured in the linear regime at low power. In this regime, the beam propagates linearly through the GRIN MMF, exciting many guided modes and producing a highly structured far-field speckle pattern. To determine the effective far-field extent of the fiber, we generated highly multimoded speckle patterns by systematically scanning the input beam position across the fiber facet. This variation in coupling conditions selectively excites different spatial modes, and summing the resulting far-field intensity patterns yields an averaged profile that captures the full spatial extent of all supported modes.

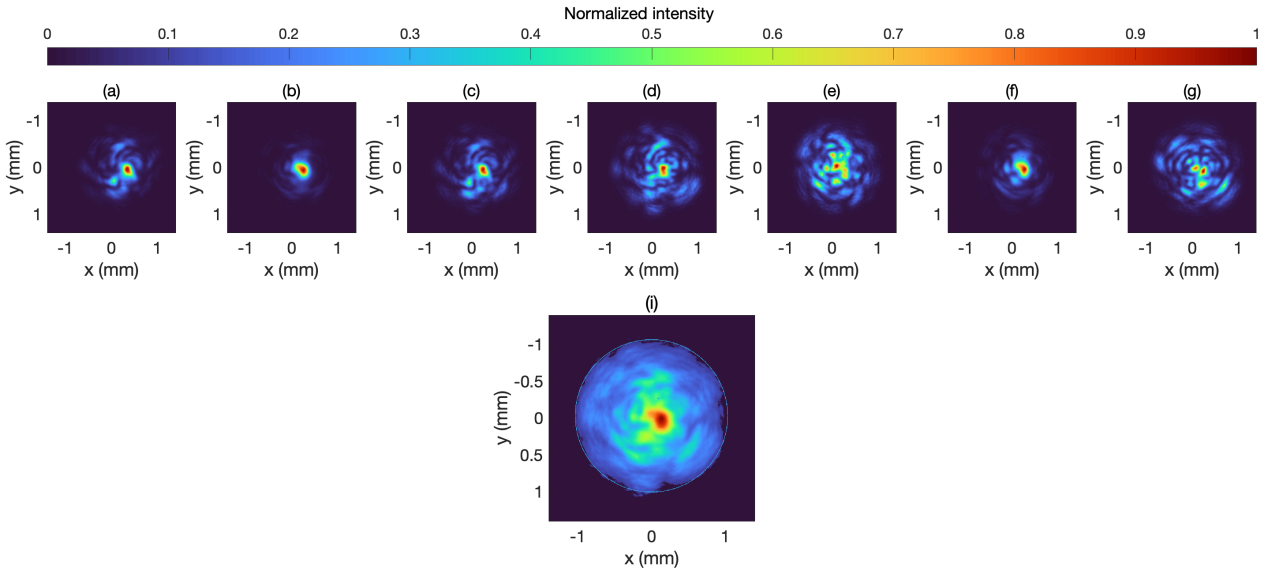

Figure 1: (a-f) Far-field speckle intensity pattern recorded at the GRIN MMF output in the linear regime (0.35 kW peak power) for different injection conditions. (i) Combined far-field speckle intensity pattern used for calibration of the scaling between camera pixels and transverse wavevector components. The blue circle marks the angular extent corresponding to the fiber core diameter projected in the far field.

The measured far-field radius was found to be 1.0212 mm, corresponding to the angular divergence of the highest-order guided mode (LP08), and was used to calibrate the spatial scaling for modal decomposition. Figure 1 shows the different far-field speckle patterns recorded for different injection conditions and modal excitations [(a)-(g)] as well as the composite representative far-field

speckle pattern [(i)] with a solid blue circle overlaid to indicate the angular extent associated with the fiber core diameter and numerical aperture. This circle defines the maximum divergence angle of the guided modes and provides a scaling reference between camera pixels and transverse wavevector components.

2. Validation of the reconstructed field

To validate the reconstructed intensity profiles obtained from digital off-axis holography, we compared the averaged reconstructed field intensity over 200 independent holograms with the corresponding raw camera intensity image acquired by blocking the reference arm. This comparison was carried out for two representative cases: in the linear propagation regime at an injected peak power of 350 W , and in the nonlinear regime at 8.3 kW. In both cases the spectral bandwidth of the reference beam was matched to that of the GRIN MMF output beam. The quantitative similarity between the two intensity maps was assessed using the structural similarity index (SI), defined as:

$$\mathrm{SI} = \frac{\sum_{x,y} I_{\mathrm{rec}}(x,y)\, I_{\mathrm{meas}}(x,y)}{\sqrt{\sum_{x,y} I_{\mathrm{rec}}(x,y)^2}\,\sqrt{\sum_{x,y} I_{\mathrm{meas}}(x,y)^2}} \times 100\%, \tag{1}$$

where $I_{\mathrm{rec}}(x,y)$ is the reconstructed intensity and $I_{\mathrm{meas}}(x,y)$ is the measured camera image intensity. As illustrated in Figure 2, the agreement is excellent in both regimes with a similarity index of $\sim$0.95 in both cases, confirming the fidelity of the reconstruction process.

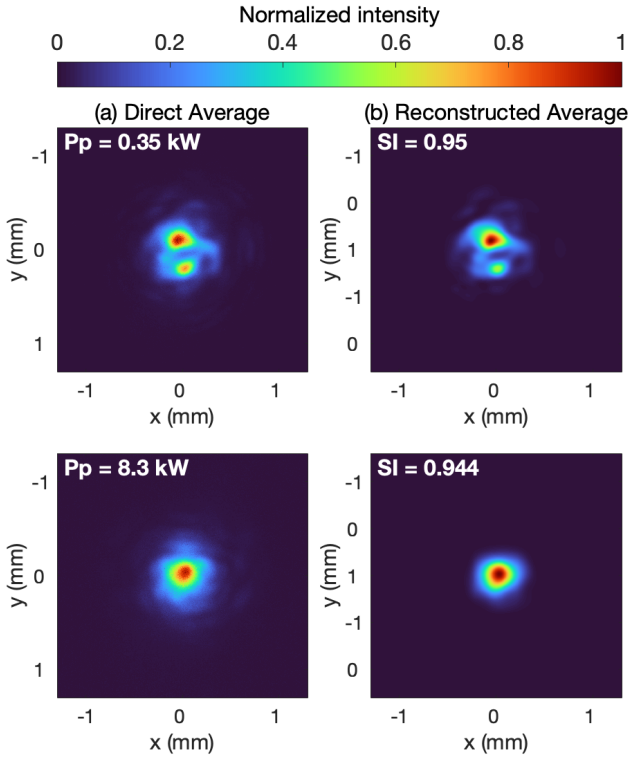

Figure 2: Comparison between the average reconstructed intensity and the measured camera image in the linear (350 W) and nonlinear (8.3 kW) regimes.

3. Spatial intensity evolution as a function of injected peak power

To illustrate how the beam evolves during the self-cleaning process, we show in Fig. 3 and Fig. 4 the reconstructed spatial intensity distributions at the output of the GRIN MMF for increasing values of injected peak power, for a reference field with narrow bandwidth corresponding to the pump residual components (Fig. 3) and a large bandwidth covering the full spectrum of the GRIN MMF beam (Fig. 4). As the power increases from the linear regime to the nonlinear regime, the speckled multimode structure gradually transitions into a smooth, centrally peaked profile correlated with spectral broadening. This progressive reshaping reflects energy transfer from higher-order modes into the fundamental mode via nonlinear interactions such as self-phase modulation and four-wave mixing. However, the spatial field corresponding to the pump residual spectral components remains highly multimoded, independently of the injected peak power.

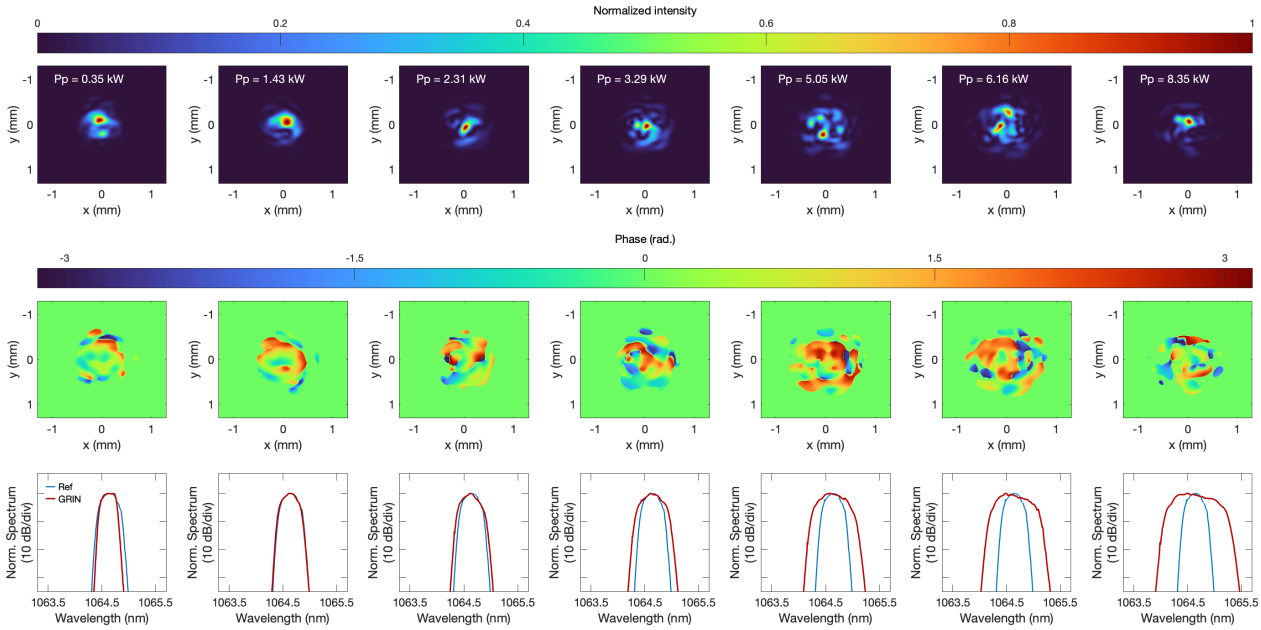

Figure 3: Reconstructed far-field at the output of the GRIN MMF for increasing injected peak powers as indicated when using a reference beam with narrow spectral bandwidth. Top row: spatial intensity, middle row: spatial phase, and bottom row: corresponding spectrum (red: GRIN MMF output and blue: reference).

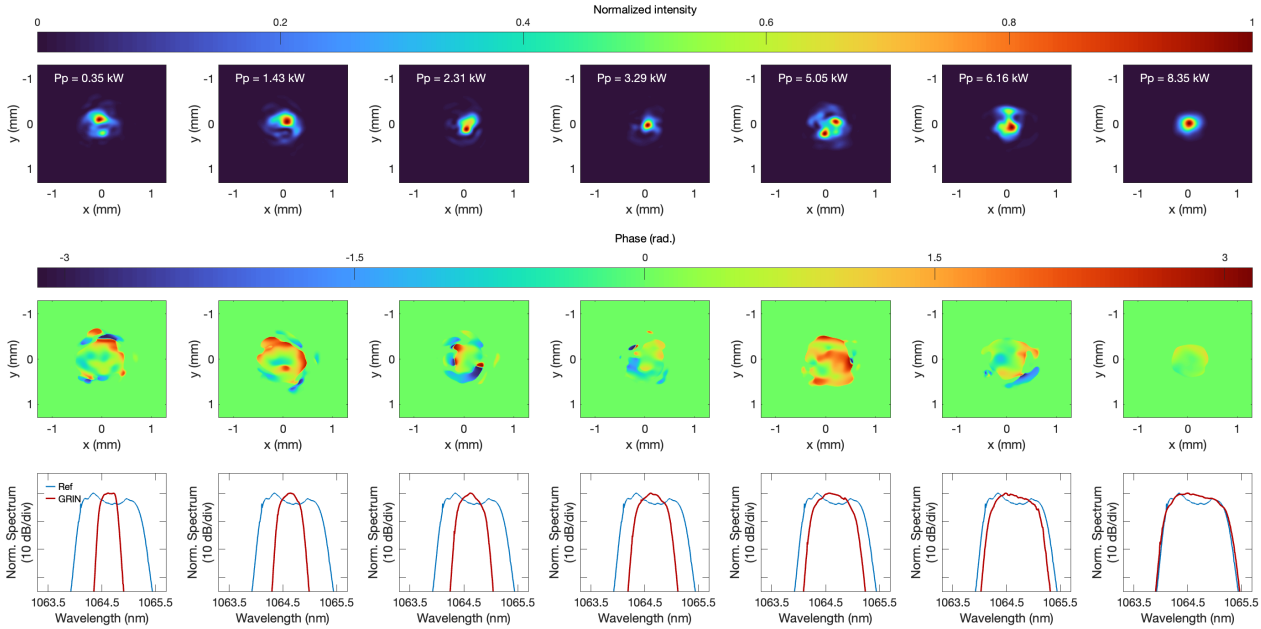

Figure 4: Reconstructed far-field at the output of the GRIN MMF for increasing injected peak powers as indicated when using a reference beam with broad spectral bandwidth. Top row: spatial intensity, middle row: spatial phase, and bottom row: corresponding spectrum (red: GRIN MMF output and blue: reference).

4. Amplitude and phase stability analysis

To characterize the shot-to-shot stability of the beam during the self-cleaning process, we analyze the standard deviations of spatial intensity and phase normalized to their mean across multiple single-shot reconstructions. This analysis reveals how deterministic and reproducible the nonlinear field evolution is at various power levels. Specifically, for each spatial point (x, y), we compute:

$$\sigma_I(x,y) = \sqrt{\langle |E(x,y)|^4 \rangle - \langle |E(x,y)|^2 \rangle^2} / \langle |E(x,y)|^2 \rangle$$

$$\sigma_\phi(x,y) = \sqrt{\langle \phi(x,y)^2 \rangle - \langle \phi(x,y) \rangle^2} / \langle \phi(x,y) \rangle$$

where $\phi(x,y) = \arg(E(x,y))$. Figures 5 and 6 present standard deviation maps of the spatial intensity (middle row) and phase (bottom row) at the GRIN MMF output for increasing injected peak power, using two different spectral filtering conditions in the holographic reference beam. Figure 4 corresponds to a narrow reference bandwidth isolating the residual pump spectrum, while Figure 5 corresponds to a broadband reference covering the full output spectrum. The top row in each figure shows the corresponding average spatial intensity. At low powers, the output field is highly multimoded and speckled, and apparent fluctuations are observed across the beam profile. However, these must be interpreted with care: in low-intensity regions, both intensity and phase fluctuations are dominated by noise and are not physically meaningful. As the peak power increases and the beam becomes more localized, the central region shows reduced fluctuation levels, reflecting enhanced stability where the intensity is highest. While both spectral filtering conditions reveal similar trends, the broadband reference in Figure 5 captures a smoother spatial structure and more localized suppression of fluctuations, particularly in the central part of the beam. However, differences at the periphery should be interpreted with care, as they arise from variation in spectral sensitivity and differences in signal-to-noise across the beam profile.

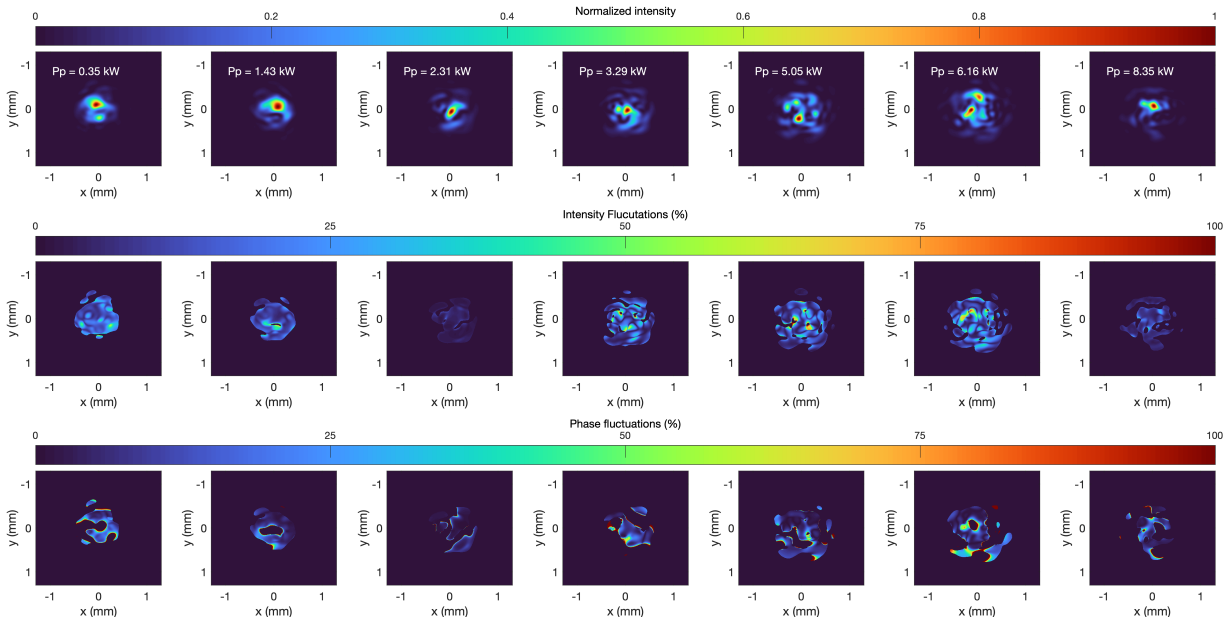

Figure 5: Standard deviation maps of spatial intensity (middle row) and phase (bottom row) for increasing peak power when using a reference beam with bandwidth corresponding to the pump residual spectrum at the GRIN MMF output. The top row shows the corresponding average spatial intensity.

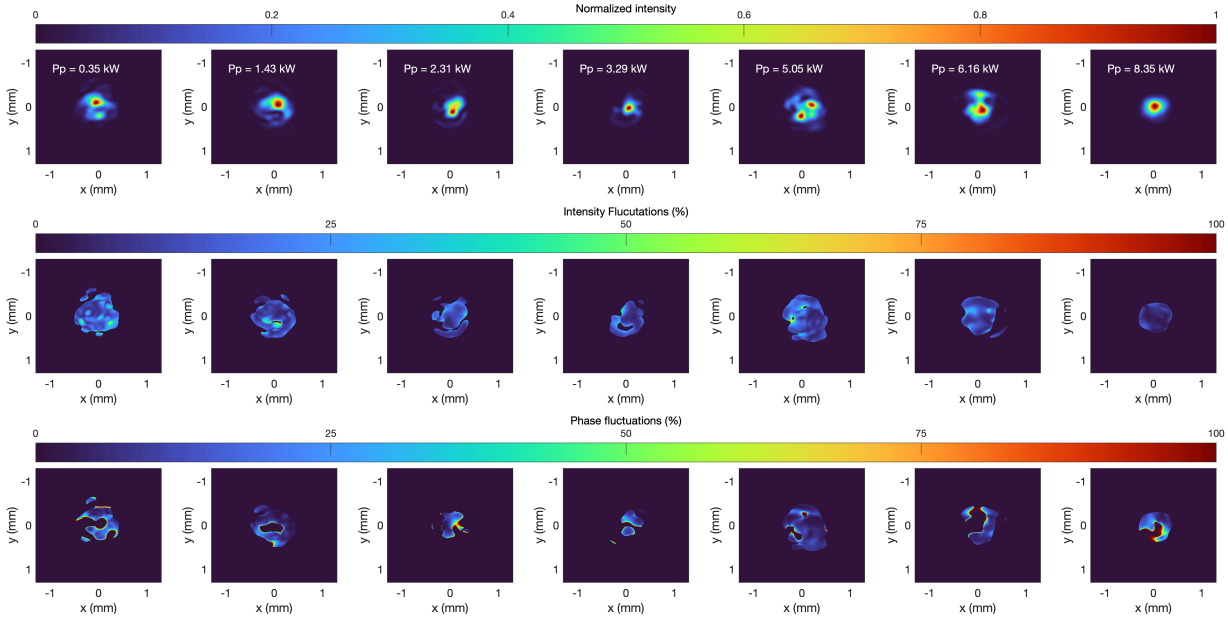

Figure 6: Standard deviation maps of spatial intensity (middle row) and phase (bottom row) for increasing peak power when using a reference beam with bandwidth covering the full spectrum of the GRIN MMF output. The top row shows the corresponding average spatial intensity.

5. Numerical simulations of spatial intensity vs. wavelength and distance

The spectrally and spatially resolved dynamics of the self-cleaning process were further characterized through numerical simulations using the multimode generalized nonlinear Schrödinger equation. The simulation results are visualized in two supplementary videos. Video 1 shows the spatial intensity distribution vs. propagation distance, integrated over the full spectral bandwidth while Video 2 illustrates the spatial intensity distribution vs. propagation distance for a 0.1 nm spectral slice centered at the pump wavelength. Video 3 shows the spatial intensity at the GRIN MMF output in an 0.1 nm spectral band centered at a wavelength as indicated. These visualizations reinforce our experimental observations and highlight the interplay between spectral reshaping and modal redistribution.